The Astrophysical Journal, 901:102 (14pp), 2020 October 1 https://doi.org/10.3847/1538-4357/abb132


# A Solar Coronal Hole and Fast Solar Wind Turbulence Model and First-orbit Parker Solar Probe (PSP) Observations

L. Adhikari[1], G. P. Zank[1,2], and L.-L. Zhao[1]
[1] Center for Space Plasma and Aeronomic Research (CSPAR), University of Alabama in Huntsville, Huntsville, AL 35899, USA
[2] Department of Space Science, University of Alabama in Huntsville, Huntsville, AL 35899, USA
*Received 2020 May 13; revised 2020 August 18; accepted 2020 August 19; published 2020 September 28*

## Abstract

We propose a turbulence-driven solar wind model for a fast solar wind flow in an open coronal hole where the solar wind flow and the magnetic field are highly aligned. We compare the numerical results of our model with Parker Solar Probe measurements of the fast solar wind flow and find good agreement between them. We find that (1) the majority quasi-2D turbulence is mainly responsible for coronal heating, raising the temperature to about $\sim 10^6$ K within a few solar radii, which leads in turn to the acceleration of the solar wind; (2) the heating rate due to quasi-2D turbulence near the coronal base is larger than that due to nearly incompressible/slab turbulence; (3) the quasi-2D energy in forward-propagating modes decreases with increasing distance, while the nearly incompressible/slab energy in forward-propagating modes increases, reaching a peak value at $\sim 11.7\ R_\odot$ before decreasing with increasing heliocentric distance; (4) the correlation length increases with increasing distance from the coronal base; and (5) the variance of the density fluctuations decreases as a function of heliocentric distance.

*Unified Astronomy Thesaurus concepts:* The Sun (1693); Solar wind (1534); Interplanetary turbulence (830)

## 1. Introduction

A primary goal of the Parker Solar Probe (PSP) mission (Fox et al. 2016) is to understand coronal heating and the origin of the fast solar wind (Matthaeus et al. 1999; Dmitruk et al. 2001; Chandran & Hollweg 2009; Cranmer & van Ballegooijen 2010; Verdini et al. 2010; Cranmer et al. 2013; Zank et al. 2018). Therefore, PSP (and the Solar Orbiter) will improve our understanding of these two problems in space physics and solar physics.

Two physical models have been suggested to describe the heating of the solar corona: "wave/turbulence-driven" (W/T) and "reconnection/loop-opening" (RLO; Cranmer & van Ballegooijen 2010). In the W/T model, magnetoconvection of open magnetic field tubes produces a broad spectral range of low-frequency magnetohydrodynamic (MHD) waves due to the transverse motion of minigranular, granular, and supergranular regions in the photosphere. The MHD waves carry kinetic and magnetic energy from the photosphere to the chromosphere and transition regions, and then into the solar corona and the distant heliosphere. The magnetic flux tubes likely originate from the intergranular regions or lanes in the quiet Sun (Fisk et al. 1999) and guide the solar wind and Alfvén waves. De Pontieu et al. (2007) suggested that transverse displacements observed in spicules can be interpreted as Alfvén waves, and related remote-sensing observations supporting the existence of Alfvén waves in the corona have been provided by Morton et al. (2016). However, the interpretation of remotely observed fluctuations as Alfvén waves has been disputed, and Erdélyi & Fedun (2007) suggest that kink modes were observed instead. The existence or not of Alfvén waves in the solar corona is not yet settled, either observationally (Tomczyk et al. 2007; Cirtain et al. 2007; Tomczyk & McIntosh 2009; Verth et al. 2011; Okamoto & De Pontieu 2011; Kuridze et al. 2012) or with respect to theory, modeling, and analysis (Zaqarashvili & Erdélyi 2009; Mathioudakis et al. 2013). The W/T model assumes that the solar wind density and magnetic field gradients cause Alfvén waves generated by transverse motion of the magnetic footpoints in the photosphere to experience non-WKB reflection (Hollweg 1986; Matthaeus et al. 1999; Zank et al. 2018). The outward- and inward-propagating Alfvén waves interact nonlinearly (Matthaeus et al. 1999), which leads to the generation of quasi-2D fluctuations (Shebalin et al. 1983) and results in the dissipation of turbulent energy. Several turbulence-driven solar wind models based on Matthaeus et al. (1999) have been used to study the acceleration of the solar wind and the heating of the coronal plasma (Dmitruk et al. 2001, 2002; Oughton et al. 2001; Suzuki & Inutsuka 2005; Cranmer et al. 2007; Chandran & Hollweg 2009; Chandran et al. 2010; Cranmer et al. 2013; Verdini et al. 2010; Woolsey & Cranmer 2014).

In the RLO model, interchange reconnection between an open flux tube and a closed loop (Moore et al. 1999; Rappazzo et al. 2012) results in the closed loop injecting hot plasma into an open flux tube. These models typically assume some form of plasma heating mechanism in the loop. Zank et al. (2018) introduced a different perspective on the RLO model in that they consider the ubiquitous magnetic carpet (Title & Schrijver 1998) that is found everywhere on the solar surface (open and closed field regions). The magnetic carpet consists of a complex admixture of magnetic field, closed and open, and polarity above the photosphere, up to the scale height of the magnetic carpet. The mixed-polarity, small-scale loops rise and interact on a replenishment timescale of about 40 hr and form a plasma region filled with largely quasi-2D turbulent fluctuations. Zank et al. (2018) focus on the small-scale loops of the magnetic carpet in open field regions and consider the actual heating process. Coronal plasma is heated by the dissipation of dynamically evolving 2D turbulence created in the magnetic carpet region through slow photospheric motions, and the turbulence is advected upward by subsonic, sub-Alfvénic flow. It is the transport of quasi-2D turbulence away from the coronal base and its subsequent dissipation that distinguishes the Zank et al. (2018) approach from the nanoflare model of Parker (Parker 1972, 1988, 1994).

Zank et al. 2018 developed a nearly incompressible MHD (NI MHD) quasi-2D and NI/slab turbulence transport model for the first time to study the evolution of turbulence in the solar atmosphere. Using fixed background profiles of solar wind density and solar wind speed, they found that the dissipation of the majority quasi-2D turbulence is sufficient to raise the temperature of the coronal plasma to millions of degrees kelvin.

Here, we develop a turbulence-driven solar wind model for the fast wind where the large-scale solar wind flow and the magnetic field are closely aligned (or antialigned). To derive the coupled quasi-2D and NI/slab turbulence transport model equations for the fast wind, we assume that the normalized NI/slab cross-helicity is equal to one and the normalized NI/slab residual energy is equal to zero. This approximation is consistent with the results of Telloni et al. (2019), who used WIND spacecraft data sets to find a $k_{||}^{-5/3}$ (where $k_{||}$ is the wavenumber along the flow direction) power spectrum for unidirectional Alfvén waves, in which the normalized cross-helicity $\sigma_c$ is equal to one. Since this result is inconsistent with critical balance theory (Goldreich & Sridhar 1995), Zank et al. (2020) present a detailed spectral theory of NI MHD to explain the origin of the observed Kolmogorov power law for unidirectional Alfvén waves. Such a power spectral density $k_{||}^{-5/3}$ has also been found by Zhao et al. (2020b) using the PSP measurements. A statistical study conducted by Stansby et al. (2019) using Helios 2 data sets finds that the anisotropic population, defined by different parallel and perpendicular solar wind proton temperatures, is almost always Alfvénic ($\sigma_c > 0.8$). Similarly, a study by Chen et al. (2020) using PSP measurements finds that the power-law index of the power spectral density of solar wind fluctuations transitions from $k^{-3/2}$ to $k^{-5/3}$ with increasing heliocentric distance. However, these studies do not consider the alignment of the velocity and the magnetic field as was done in Telloni et al. (2019) and Zhao et al. (2020b). Here, we develop a turbulence model that incorporates unidirectional Alfvén waves by coupling the nearly incompressible turbulence model equations (Zank et al. 2017) with a background plasma described by the continuity, momentum, and energy equations that incorporates turbulent heating. In deriving the turbulence-driven solar wind model equations for the fast solar wind flow, we assume that the NI/slab component is highly Alfvénic so that the fluctuating kinetic and magnetic energy are equipartitioned (i.e., the normalized residual energy is equal to zero) and the normalized cross-helicity is equal to one (Adhikari et al. 2019b; Parashar et al. 2020; Zhao et al. 2020a). We compare the theoretical solutions with PSP measurements of the fast solar wind flow.

In Adhikari et al. (2020), we studied the evolution of turbulence in the slow solar wind between the perihelion of the first orbit of PSP and 131.64 $R_\odot$. We found good agreement between the theoretical results and the slow wind observed by PSP Solar Wind Electrons Alphas and Protons (SWEAP; Kasper et al. 2016). Therefore, this study may identify distinguishing differences between turbulence in the fast solar wind and that in the slow solar wind.

We select four intervals with start and end times (DOY:HR:MN) of (312:13:0.378–313:8:46.54), (318:1:56.62–319:5:54.51), (319:21:25.64–321:7:59.89), and (323:7:7.16—324.0.46:27.35). These are roughly one-day intervals during which the radial component of the solar wind speed is approximately constant, indicating that the plasma is not perturbed (Borovsky 2016). Although the plasma in the selected intervals may not originate from the same coronal hole (Badman et al. 2020), these intervals should illustrate the general trend of the evolution of turbulence in the fast solar wind. We will therefore compare the model results with PSP measurements to gauge the effectiveness of our turbulence-driven coronal heating and solar wind model. The selected interval corresponds to the fast solar wind flow observed by PSP during its first encounter in the outbound direction. The plasma data are moment data from the PSP SWEAP measurements (Kasper et al. 2016).

The top and middle panels of Figure 1 show the 4 hr averaged R, T, and N components of the solar wind speed and the magnetic field of the selected interval. Also shown is the angle between the mean solar wind speed and the magnetic field ($\theta_{UB}$) as a function of heliocentric distance.

We see that the large-scale mean flow and the magnetic field are mostly aligned or antialigned: the bottom panel of Figure 1 shows a histogram of the $\theta_{UB}$. During the second orbit, PSP observed mostly slow solar wind. The PSP magnetometer and plasma data are obtained from the website https://cdaweb.gsfc.nasa.gov/index.html/.

We organize the manuscript as follows. In Section 2, we present the turbulence-driven solar wind model for the field-aligned solar wind flow. Section 3 discusses the results and a comparison of the results with PSP measurements. Finally, Section 4 presents a discussion and conclusions.

## 2. A Turbulence-driven Solar Wind Model

The nearly incompressible description of MHD turbulence successfully describes the observed turbulent behavior of the solar wind plasma. According to a nearly incompressible description, the incompressible equations for the $\beta_p \gg 1$ regime (where $\beta_p \equiv 2nk_{\rm B}T/(B^2/2\mu_0)$, $n$ is the solar wind density, $k_{\rm B}$ is Boltzmann's constant, $T$ is the solar wind temperature, $B$ is the large-scale magnetic field, and $\mu_0$ is the magnetic permeability) are fully 3D (Zank & Matthaeus 1992, 1993; Zank et al. 2012), while the leading-order incompressible equations in the $\beta_p \ll 1$ and $\sim 1$ regime are quasi-2D, and the higher-order corrections are fully 3D (Hunana & Zank 2010; Zank et al. 2017). Here the fully 3D refers to a function in $x$, $y$, and $z$, and quasi-2D refers to a function in $x$ and $y$, that is, in a plane perpendicular to the direction of the magnetic field. The leading-order (quasi-2D) and higher-order corrections (NI/slab) can be expressed in terms of the Elsässer variables as

$$\boldsymbol{z}^{\infty\pm} = \boldsymbol{u}^{\infty} \pm \frac{\boldsymbol{B}^{\infty}}{\sqrt{\mu_0\rho}} \text{ and } \boldsymbol{z}^{*\pm} = \boldsymbol{u}^{*} \pm \frac{\boldsymbol{B}^{*}}{\sqrt{\mu_0\rho}}, \quad (1)$$

respectively, where the superscripts $\infty$ and $^*$ refer to quasi-2D and NI/slab turbulence. Zank et al. (2020) showed that the NI MHD equations in the $\beta_p \sim 1$ or $\ll 1$ regime in an inhomogeneous (homogeneous) flow comprise a leading-order component of a quasi-2D (2D) component and NI compressible corrections that include both slab (counterpropagating Alfvén waves) and higher-order quasi-2D fluctuations. The parameters $\boldsymbol{u}^{\infty,*}$ and $\boldsymbol{B}^{\infty,*}$ are the fluctuating velocity and magnetic field, and $\rho$ is the solar wind mass density. The quasi-2D component is typically assumed to be isotropic in the 2D plane perpendicular to the magnetic field, although that is not necessarily true, while the higher-order description admits both a quasi-2D and an axisymmetric (slab) component with a particular direction $\hat{s}$

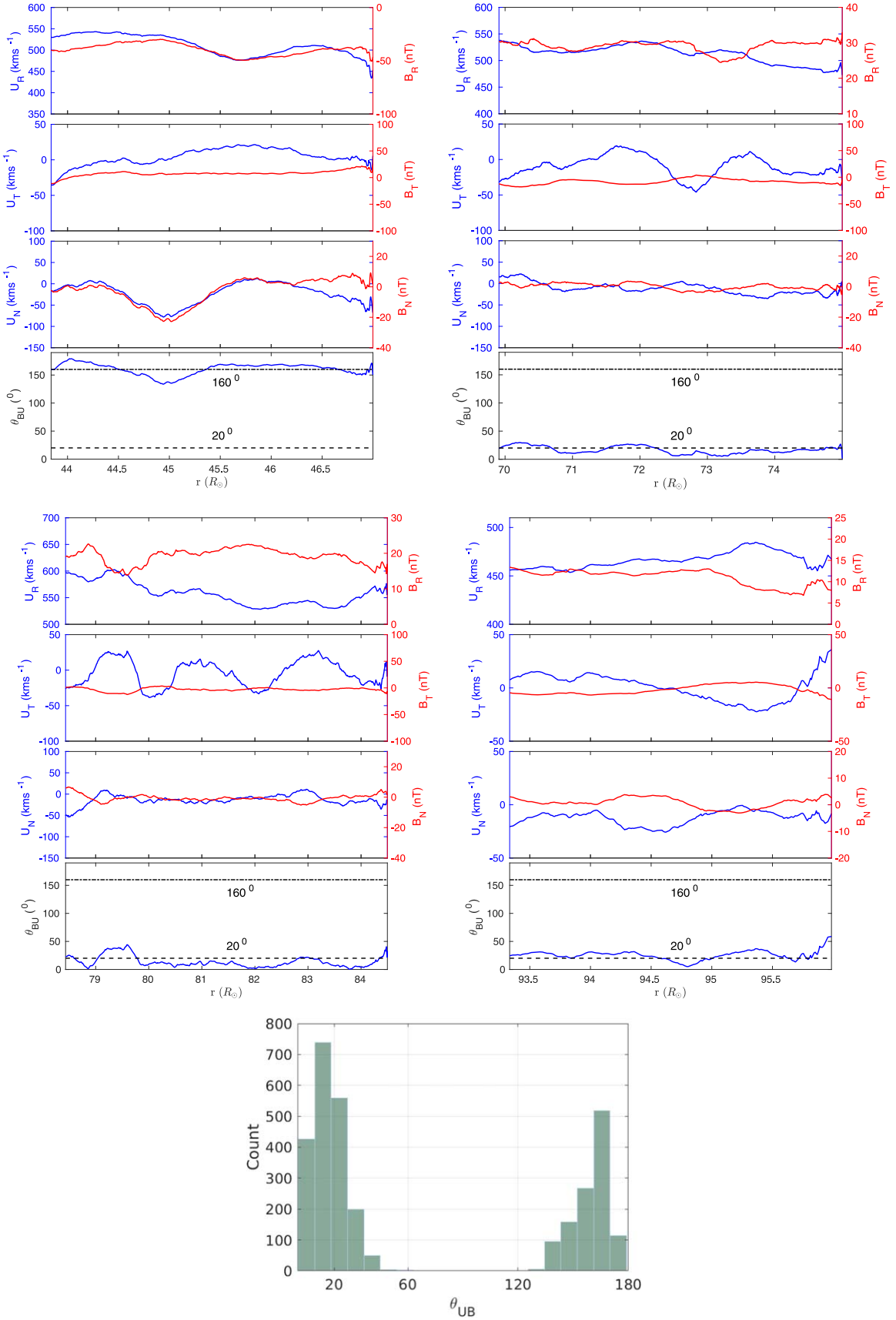


**Figure 1.** Top left and right and middle left and right are the R, T, and N components of the solar wind speed and magnetic field for the fast solar wind observed at different heliocentric distances, and the angle between the large-scale solar wind speed and the magnetic field ($\theta_{UB}$). Bottom: histogram of the angle between the large-scale solar wind speed and the magnetic field.

defined by the magnetic field. Therefore, NI MHD represents a combination of isotropic and axisymmetric turbulence in the order of one or a small plasma beta limit.

We couple the NI MHD turbulence model with the background plasma via turbulent heating of the plasma. The background plasma is described by the mass and momentum equations and the solar wind temperature equation and is given in the 1D steady-state spherically symmetric coordinate system as

$$\frac{d}{dr}(r^2\rho U) = 0; \tag{2}$$

$$\rho U\frac{dU}{dr} = -\frac{dP}{dr} - \frac{GM_\odot\rho}{r^2}; \tag{3}$$

$$\begin{aligned} U\frac{dT}{dr} &= -(\gamma-1)T\frac{dU}{dr} - (\gamma-1)\frac{2UT}{r} + \frac{s_1}{3}\frac{m_p}{k_B}\alpha \\ &\times\left[2\frac{\langle z^{*+2}\rangle\langle z^{\infty+2}\rangle\langle z^{\infty-2}\rangle^{1/2}}{L_\infty^+}\right. \\ &+ 2\frac{\langle z^{\infty+2}\rangle^2\langle z^{\infty-2}\rangle^{1/2}}{L_\infty^+} + 2\frac{\langle z^{\infty-2}\rangle^2\langle z^{\infty+2}\rangle^{1/2}}{L_\infty^-} \\ &\left.+ E_D^\infty\left(\frac{\langle z^{\infty+2}\rangle\langle z^{\infty-2}\rangle^{1/2}}{L_\infty^+} + \frac{\langle z^{\infty-2}\rangle\langle z^{\infty+2}\rangle^{1/2}}{L_\infty^-}\right)\right], \end{aligned} \tag{4}$$

where $U$ is the solar wind speed, $P$ the thermal pressure, $G$ the gravitational constant, $M_\odot$ the solar mass, $m_p$ the proton mass, $n$ the solar wind density, and $k_B$ Boltzmann's constant. The third term on the right-hand side (rhs) of Equation (4) is the turbulent heating term through which the solar wind equations are coupled with the quasi-2D and NI/slab turbulence transport model equations. Although these solar wind equations do not include the magnetic field, they differ from the original Parker model (Parker 1958) through the presence of the turbulent heating term. In addition, the Parker model assumes an isothermal plasma with $\gamma = 1$, while we assume $\gamma = 5/3$. In Equation (4), the parameter $\alpha$ is the von Kármán–Taylor constant and determines the dissipation rate of turbulence. Various values for $\alpha$ have been used in prior studies. Matthaeus et al. (1999) use $\alpha = 1$ in their model of coronal heating by magnetohydrodynamic turbulence. Vasquez et al. (2007) and Montagud-Camps et al. (2018) use a value of $\alpha$ that is about 1/10 in the heliosphere. Bandyopadhyay et al. (2020) use an even smaller value, taking $\alpha = 0.03$ in their analysis of the energy transfer rate observed by PSP. It has also been argued that a constant factor may not be a good approximation in the sub-Alfvénic solar wind regime (van Ballegooijen & Asgari-Targhi 2016). In our analysis, we use $\alpha = 0.07$. In Equation (4), the parameter $s_1$ denotes the fraction of the turbulent energy that heats the coronal/solar wind plasma. In our study, we choose $s_1 = 0.8$, in other words, that 80% of the turbulent energy heats the solar wind coronal plasma in the fast solar wind. Some fraction of the turbulence energy is expected to go into creating a nonthermal ion population (possibly as a result of some form of stochastic acceleration by magnetic islands, e.g., Zank et al. 2014; Zhao et al. 2018b, 2019; Adhikari et al. 2019a), and some fraction goes into creating a nonthermal electron population. Further study is needed to determine what fraction of the turbulence energy heats solar wind protons and electrons, and what fraction of the turbulence energy creates nonthermal populations of ions and electrons.

The magnetic field $\boldsymbol{B}$ is assumed to be radial and is given by

$$\boldsymbol{B} = B_0\left(\frac{r_0}{r}\right)^2\hat{r},$$

where the subscript 0 denotes an arbitrary reference point and $\hat{r}$ is the direction of the magnetic field. Although the model assumes that the magnetic field expands completely radially, it should be recognized that the coronal magnetic field tends to overexpand in the corona (Kopp & Holzer 1976).

In the momentum Equation (3), the first term on the rhs is the pressure gradient, and the second term is the gravitational force. In this model, the pressure gradient is the only force driving the solar wind from subsonic to supersonic. Other driving forces, such as the ponderomotive force (see Holzer & Axford 1970; Leer et al. 1982; Withbroe 1988; Fisk et al. 1999; Cranmer & van Ballegooijen 2010; Verdini et al. 2010; Cranmer et al. 2013) or wave pressure (McKenzie et al. 1995), are not included in the current model. Fisk et al. (1999) pointed out that the wave pressure of the Alfvénic fluctuations can be ignored when the particle pressure P generated is larger than any possible wave pressure or ponderomotive force caused by magnetic energy density $\langle B^2\rangle/(2\mu_0)$ (see also Verdini et al. 2010), because the radial magnetic field exerts no direct force on the mean flow (see Fisk et al. 1999). Although the ponderomotive force can affect the solar wind flow, it is not as important as the pressure gradient. We will address this problem in the future. In the model presented here, the pressure gradient is the main force driving the solar wind within a few solar radii because it is generated by a hot coronal plasma with a temperature of about $10^6$ K. Our approach to heating the corona through the dissipation of turbulence (i.e., the third term on the rhs of Equation (4)) is different from that of Habbal et al. (1995), who expressed the heating term in an exponential form, $h = h_0\exp(-(r-r_1)/\lambda)$, where $h_0$ is the strength of the heating term, $\lambda$ is a dissipation length scale, $r$ is heliocentric distance, and $r_1 \sim 2$ solar radii. From Equations (2), (3), and (4), we can derive the following equation:

$$\begin{aligned} \frac{C_s^2}{U}(M_s^2-1)\frac{dU}{dr} &= \frac{4\gamma k_B}{m_p}\frac{T}{r^2}\left[r - \frac{GM_\odot m_p}{4\gamma k_B}\frac{1}{T}\right. \\ &- \frac{\alpha s_1 m_p}{6\gamma k_B}\frac{r^2}{UT}\left\{2\frac{\langle z^{*+2}\rangle\langle z^{\infty+2}\rangle\langle z^{\infty-2}\rangle^{1/2}}{L_\infty^+}\right. \\ &+ 2\frac{\langle z^{\infty+2}\rangle^2\langle z^{\infty-2}\rangle^{1/2}}{L_\infty^+} + 2\frac{\langle z^{\infty-2}\rangle^2\langle z^{\infty+2}\rangle^{1/2}}{L_\infty^-} \\ &\left.\left.+ E_D^\infty\left(\frac{\langle z^{\infty+2}\rangle\langle z^{\infty-2}\rangle^{1/2}}{L_\infty^+} + \frac{\langle z^{\infty-2}\rangle\langle z^{\infty+2}\rangle^{1/2}}{L_\infty^-}\right)\right\}\right], \end{aligned} \tag{5}$$

where $M_s = U/C_s$ is the sonic Mach number, and $C_s^2 = 2\gamma k_B T/m_p$ is the square of the sound speed. Equation (5) is the solar wind equation, showing that the solar wind speed is a function of solar wind parameters and turbulent quantities, indicating that turbulence influences the solar wind speed. In addition, when the left-hand side terms in parentheses (...) and the right-hand side terms in the square brackets [....] are zero simultaneously, Equation (5) possesses a sonic point. This is a

case when the sound speed is equal to the solar wind speed. To solve Equation (5) near the sonic point, we use L'Hôpital's rule.

As discussed above, the solar wind equations couple with the quasi-2D and NI/slab turbulence transport model equations through the third term on the right-hand side of Equation (4) or (5). This term consists of quasi-2D and NI/slab variances of the Elsässer variables, the quasi-2D residual energy, and the quasi-2D correlation functions corresponding to forward- and backward-propagating modes. The Elsässer energies and the residual energies are defined as (Zank et al. 2012, 2017)

$$\langle z^{\infty,*\pm 2}\rangle = \langle \boldsymbol{z}^{\infty,*\pm}\cdot \boldsymbol{z}^{\infty,*\pm}\rangle;\ E_D^{\infty,*} = \langle \boldsymbol{z}^{\infty,*+}\cdot \boldsymbol{z}^{\infty,*-}\rangle, \quad (6)$$

where $\langle . \rangle$ denotes an ensemble average, in the usual mean field sense as done typically in turbulence theory (see McComb 1995). The turbulence transport model equations (Equations (8)–(13)) describe the evolution of turbulence from the surface of the Sun to the outer heliosphere. We give the boundary conditions for the turbulent quantities and solve the turbulence transport model equations by a Runge–Kutta fourth-order method. Similarly, the correlation functions corresponding to Elsässer variables and the residual energy can be written as (Zank et al. 2012, 2017)

$$\begin{aligned} L_{\infty,*}^{\pm} &= \int \langle \boldsymbol{z}^{\infty,*\pm}\cdot \boldsymbol{z}^{\infty,*\pm}\rangle dx \equiv \langle z^{\infty,*\pm 2}\rangle \lambda_{\infty,*}^{\pm};\\ L_D^{\infty,*} &= \int \langle \boldsymbol{z}^{\infty,*+}\cdot \boldsymbol{z}^{\infty,*-\prime} + \boldsymbol{z}^{\infty,*+\prime}\cdot \boldsymbol{z}^{\infty,*-}\rangle dx\\ &\equiv E_D^{\infty,*}\lambda_D^{\infty,*}, \end{aligned} \quad (7)$$

where $\boldsymbol{z}^{\infty,*\pm\prime}$ represents the lagged Elsässer variables. The parameters $\lambda_{\infty,*}^{\pm}$ and $\lambda_D^{\infty,*}$ are the correlation lengths corresponding to the quasi-2D and NI/slab Elsässer variables and the residual energy.

The evolution of the majority quasi-2D turbulence can be expressed by the 1D steady-state turbulence transport model equations in a spherically symmetric coordinate system as (Zank et al. 2017, 2018; Adhikari et al. 2017, 2019c)

$$\begin{aligned} &U\frac{d\langle z^{\infty\pm 2}\rangle}{dr} + \frac{1}{2}(\langle z^{\infty\pm 2}\rangle + E_D^{\infty})\left(\frac{dU}{dr} + \frac{2U}{r}\right)\\ &\quad = -2\alpha\frac{\langle z^{\infty\pm 2}\rangle^2\langle z^{\infty\mp 2}\rangle^{1/2}}{L_{\infty}^{\pm}}; \end{aligned} \quad (8)$$

$$\begin{aligned} &U\frac{dE_D^{\infty}}{dr} + \frac{1}{2}(E_D^{\infty} + E_T^{\infty})\left(\frac{dU}{dr} + \frac{2U}{r}\right)\\ &\quad = -\alpha E_D^{\infty}\left(\frac{\langle z^{\infty+2}\rangle\langle z^{\infty-2}\rangle^{1/2}}{L_{\infty}^{+}} + \frac{\langle z^{\infty-2}\rangle\langle z^{\infty+2}\rangle^{1/2}}{L_{\infty}^{-}}\right); \end{aligned} \quad (9)$$

$$U\frac{dL_{\infty}^{\pm}}{dr} + \frac{1}{2}\left(L_{\infty}^{\pm} + \frac{L_D^{\infty}}{2}\right)\left(\frac{dU}{dr} + \frac{2U}{r}\right) = 0; \quad (10)$$

$$U\frac{dL_D^{\infty}}{dr} + \frac{1}{2}\left(\frac{dU}{dr} + \frac{2U}{r}\right)(L_D^{\infty} + L_{\infty}^{+} + L_{\infty}^{-}) = 0, \quad (11)$$

where $E_T^{\infty} = (\langle z^{\infty+2}\rangle + \langle z^{\infty-2}\rangle)/2$ is the quasi-2D total turbulent energy. The right-hand sides of Equations (8) and (9) differ from the right-hand sides of Equations (8) and (9) of Zank et al. (2018; see also Zank et al. 2017; Adhikari et al. 2017) in the source term associated with NI/slab turbulence. This term is absent in the above equations because the backward-propagating minority energy $\langle z^{*-2}\rangle = 0$, because we assume that the NI/slab normalized cross-helicity is equal to one ($\sigma_c^* = 1$) and that the NI/slab normalized residual energy is equal to zero ($\sigma_D^* = 0$). We choose these conditions for the minority NI/slab turbulence because it includes propagating Alfvén waves. On assuming Alfvénicity, the two coupled Equations (18) and (21) derived in the Appendix describe the evolution of NI/slab turbulence. Therefore, unlike the 12 coupled quasi-2D and NI/slab turbulence transport equations in Zank et al. (2018; see also Zank et al. 2017; Adhikari et al. 2017), we now have only eight coupled quasi-2D and NI/slab turbulence transport equations. Equation (18) is the transport equation for the energy in forward waves, and Equation (21) is the transport equation for the correlation function corresponding to forward waves. Equations (18) and (21) can be written in a 1D steady-state spherically symmetric coordinate system as (Zank et al. 2017, 2018; Adhikari et al. 2017)

$$\begin{aligned} &(U - V_A)\frac{d\langle z^{*+2}\rangle}{dr} + \frac{1}{2}\frac{dU}{dr}\langle z^{*+2}\rangle\\ &\quad - (2b-1)\frac{U}{r}\langle z^{*+2}\rangle - \frac{1}{2}\frac{V_A}{\rho}\frac{d\rho}{dr}\langle z^{*+2}\rangle\\ &\quad = -2\alpha\frac{\langle z^{*+2}\rangle\langle z^{\infty+2}\rangle\langle z^{\infty-2}\rangle^{1/2}}{L_{\infty}^{+}}; \end{aligned} \quad (12)$$

$$\begin{aligned} &(U - V_A)\frac{dL_*^{+}}{dr} + \frac{1}{2}\frac{dU}{dr}L_*^{+}\\ &\quad - (2b-1)\frac{U}{r}L_*^{+} - \frac{1}{2}\frac{V_A}{\rho}\frac{d\rho}{dr}L_*^{+} = 0, \end{aligned} \quad (13)$$

where $V_A = B/\sqrt{\mu_0\rho}$ is the Alfvén velocity. The parameter $b$ defines the geometry of the NI/slab turbulence. We use $b = 0.26$ (see Zank et al. 2012, 2017 for details regarding this choice) to ensure reasonable numerical solutions of the turbulence-driven solar wind model. Equations (8)–(13) are a set of turbulence transport equations that describe the evolution of turbulence in the highly Alfvénic solar wind plasma. In this system, the energy of outwardly propagating Alfvén waves is dissipated via its interaction with quasi-2D turbulence (Zank et al. 2017), as indicated by the right-hand side of Equation (12). This results in a Kolmogorov-type power spectral density for wavenumbers parallel to the magnetic field aligned flow, that is, $k_{||}^{-5/3}$ (Zank et al. 2020), as observed in the solar wind (Telloni et al. 2019) and solar corona (Zhao et al. 2020b). These results indicate that NI/slab turbulence does not turn off even when only unidirectional Alfvén waves are present (Adhikari et al. 2019b). The model presented here couples the quasi-2D and NI/slab turbulence transport model Equations (8)–(13) when the normalized NI/slab cross-helicity is equal to one ($\sigma_c^* = 1$), and the normalized NI/slab residual energy is equal to zero ($\sigma_D^* = 0$).

The evolution of turbulence affects the evolution of the variance of the solar wind density fluctuations in the NI MHD theory and can be expressed by the 1D steady-state transport

**Table 1**
Boundary Values at 1 $R_\odot$ for Turbulent Quantities and Solar Wind Parameters

| Parameters | Values | Parameters | Values |
|---|---|---|---|
| $\langle z^{\infty+2}\rangle$ (km$^2$ s$^{-2}$) | $5.8 \times 10^5$ | $\langle z^{*-2}\rangle$ (km$^2$ s$^{-2}$) | 1100 |
| $\langle z^{\infty-2}\rangle$ (km$^2$ s$^{-2}$) | $5.8 \times 10^5$ | $L_*^+$ (km$^3$ s$^{-2}$) | $1.76 \times 10^8$ |
| $E_D^\infty$ (km$^2$ s$^{-2}$) | 2000 | $U$ (km s$^{-1}$) | 13.56 |
| $L_\infty^+$ (km$^3$ s$^{-2}$) | $4.64 \times 10^{10}$ | $n$ (cm$^{-3}$) | $1.0 \times 10^7$ |
| $L_\infty^-$ (km$^3$ s$^{-2}$) | $4.64 \times 10^{10}$ | $T$ (K) | $5 \times 10^5$ |
| $L_D^\infty$ (km$^3$ s$^{-2}$) | $1.6 \times 10^8$ | $\langle \rho^{\infty 2}\rangle$ (cm$^{-6}$) | $2 \times 10^{11}$ |

equation as (Zank et al. 2017; Adhikari et al. 2017)

$$U\frac{d\langle\rho^{\infty 2}\rangle}{dr} + 2\langle\rho^{\infty 2}\rangle\frac{dU}{dr} + 4\frac{U}{r}\langle\rho^{\infty 2}\rangle = -\alpha\frac{\langle u^{\infty 2}\rangle^{1/2}\langle\rho^{\infty 2}\rangle}{l_u^\infty}, \quad (14)$$

where $\langle u^{\infty 2}\rangle = (\langle z^{\infty+2}\rangle + \langle z^{\infty-2}\rangle + 2E_D^\infty)/4$ is the quasi-2D fluctuating kinetic energy, and $l_u^\infty = [(E_T^\infty + E_C^\infty)\lambda_\infty^+ + (E_T^\infty - E_C^\infty)\lambda_\infty^- + E_D^\infty\lambda_D^\infty]/2(E_T^\infty + E_D^\infty)$ is the correlation length of the quasi-2D fluctuating kinetic energy. The parameter $E_C^\infty$ is the quasi-2D cross-helicity. Equation (14) shows that the variance of the density fluctuations interacts with the quasi-2D turbulent kinetic energy in a passive scalar sense, and this interaction is responsible for a decrease in the variance of the density fluctuations. Equation (14) indicates that the density variance exhibits different radial profiles, depending on whether the quasi-2D residual energy satisfies $E_D^\infty = 0$, $E_D^\infty < 0$, and $E_D^\infty > 0$. Zank et al. (2017) showed that the variance of density fluctuations follows different radial profiles in the case when the solar wind fluctuations are dominated by the turbulent kinetic energy than when they are dominated by the turbulent magnetic energy.

We study the evolution of solar wind turbulence in the fast wind by solving the coupled solar wind and turbulence transport model equations and using PSP fast wind measurements. We solve the coupled transport equations with the boundary conditions shown in Table 1 using a Runge–Kutta fourth-order method. To derive the boundary conditions for the quasi-2D Elsässer variables, we follow an analysis similar to that of Zank et al. (2018; see also De Pontieu et al. 2007; Moore et al. 2015).

The boundary condition for the NI/slab turbulence energy is chosen in such a way that the NI/slab turbulence energy does not exceed the quasi-2D turbulence energy because the latter is the dominant component in our turbulence model. The correlation length for the quasi-2D turbulence is assumed to be $\lambda_\infty = 8 \times 10^4$ km, which is 16 times larger than that found by Abramenko et al. (2013) at the coronal base. We also assume that the correlation length of the quasi-2D residual energy is equal to $\lambda_\infty$, and the correlation length for the NI/slab turbulence is $2\lambda_\infty$. In Table 1, the boundary conditions at the coronal base are chosen in such a way that the numerical solutions of the model are reasonable and yield results consistent with PSP measurements.

## 3. Results: Numerical Solutions of the Model Equations

We present numerical solutions of the turbulence-driven solar wind model equations, and we compare them with PSP measurements.

Figure 2(a) compares the theoretical and observed solar wind speed, Alfvén velocity, and sound speed as a function of heliocentric distance. The observed quantities are shown by red diamonds with error bars. The error bars represent the interquartile range. The solar wind speed (solid curve) increases from 13.56 km s$^{-1}$ at the coronal base to ~370 km s$^{-1}$ at ~4 $R_\odot$, and then it increases more slowly and monotonically as $\sim r^{0.14}$ with increasing heliocentric distance. The theoretical and observed solar wind speeds between 35.5 $R_\odot$ and 100 $R_\odot$ are basically the same. The Alfvén velocity (dashed curve, see the inset) increases from 900 km s$^{-1}$ at the coronal base to $2.79 \times 10^3$ km s$^{-1}$ at about 1.2 $R_\odot$ and then decreases with increasing heliocentric distance. This result shows that the Alfvén surface forms at a heliocentric distance of ~11.7 $R_\odot$. The position of the Alfvén surface can be influenced by the turbulence level in the solar atmosphere. In Figure 2(a), the blue diamonds indicate the observed Alfvén velocity. Similar to the Alfvén velocity, the sound speed (dashed–dotted–dashed curve, see the inset) also increases initially and then decreases with increasing heliocentric distance. The sound speed and the solar wind speed intersect at ~1.78 $R_\odot$, the sonic point.

Figure 2(b) shows the solar wind proton temperature as a function of heliocentric distance. From the base of the solar corona, the proton temperature increases from $5 \times 10^5$ K to $\sim 3.5 \times 10^6$ K within 2 $R_\odot$, and then decreases monotonically with increasing heliocentric distance (see the inset). This increase in the solar wind proton temperature from $5 \times 10^5$ K to $\sim 3.5 \times 10^6$ K within a few solar radii is a consequence of the rapid dissipation of quasi-2D turbulence (see Figure 3(a)). As the coronal plasma is heated to millions of degrees kelvin, the pressure gradient becomes so large that the accelerating coronal plasma transits from a subsonic state (i.e., $|U| < C_S$) to a supersonic state (i.e., $|U| > C_S$) within 2 $R_\odot$. The red diamonds indicate the observed solar wind proton temperature, which exhibits a power law of $\sim r^{-1.25}$ in heliocentric distance. Compared to the observed proton temperature of the slow solar wind measured by PSP during its first perihelion from 35.5 $R_\odot$ to 131.64 $R_\odot$ (Figure 3(b) in Adhikari et al. 2020), the observed proton temperature of the fast solar wind is comparatively large, and the cooling rate of the temperature in the fast solar wind is faster than that of the cooling rate in the slow solar wind where the proton temperature exhibits a power law of $\sim r^{-0.95}$ (Adhikari et al. 2020). In the slow solar wind plasma, turbulence is fully developed, and the presence of a stream-shear source of turbulence reduces the rate of decrease of the solar wind proton temperature. In Figure 2(b), the theoretical solar wind proton temperature is approximately similar to the observed solar wind proton temperature between ~35 $R_\odot$ and ~50 $R_\odot$, but it is somewhat higher between 70 $R_\odot$ and 100 $R_\odot$.

Figure 2(c) shows a comparison between the theoretical and observed solar wind densities as a function of heliocentric distance. The theoretical solar wind density at the base of the solar corona is assumed to be $10^7$ cm$^{-3}$, which decreases by two orders within 2 $R_\odot$ and then more gradually with increasing heliocentric distance. The rapid decrease of the solar wind proton density is a consequence of the acceleration of the solar wind speed. The red diamonds show the observed

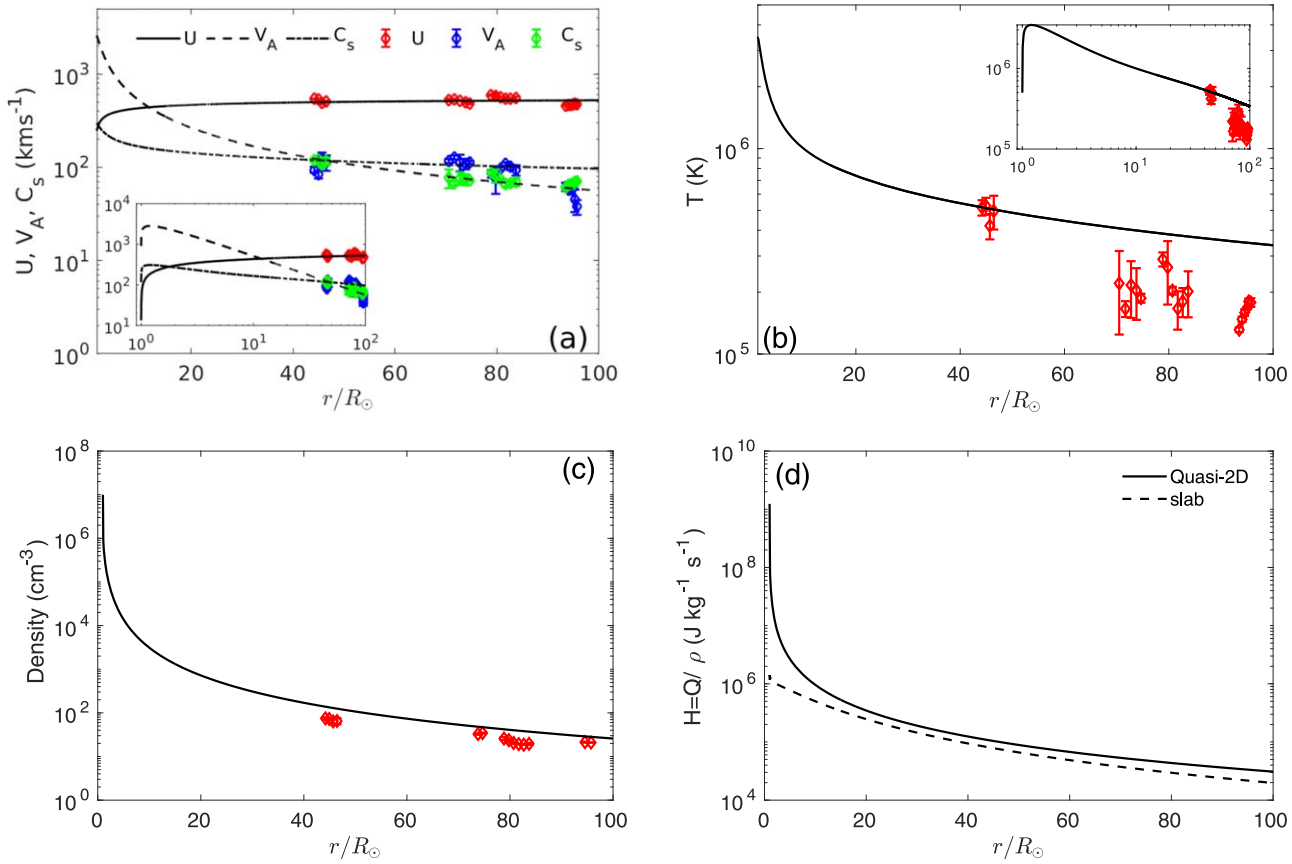


**Figure 2.** The panels show (a) the solar wind speed (solid curve), the Alfvén speed (dashed curve), and the sound speed (dashed–dotted–dashed curve); (b) the solar wind proton temperature (solid curve); (c) the solar wind density (solid curve); and (d) the heating rate of quasi-2D (solid curve) and NI/slab (dashed curve) turbulence as a function of heliocentric distance. The red diamonds denote the corresponding observed solar wind parameters with error bars.

solar wind density of the fast solar wind flow, which follows a power law of $r^{-2.14}$ between 35.5 $R_\odot$ and 100 $R_\odot$. This power law also confirms that the solar wind speed increases because the solar wind density decreases more rapidly than $r^{-2}$. The theoretical and observed solar wind proton density radial profiles are similar. Figure 2(d) displays the heating rates of quasi-2D and slab turbulence as a function of heliocentric distance. The heating rate of quasi-2D turbulence at the base of the solar corona is $\sim 10^3$ orders of magnitude greater than that of the slab turbulence, and it decreases rapidly near the coronal base. The heating rate for quasi-2D turbulence decreases by two orders within 2 $R_\odot$ and then decreases more gradually as $r^{-1.5}$, while the heating rate for slab turbulence decreases as $r^{-1.1}$. This result shows that quasi-2D turbulence provides most of the energy to heat the coronal plasma to millions of degrees kelvin and to accelerate the solar wind speed from a subsonic to supersonic state.

Figure 3(a) shows the evolution of quasi-2D (solid curve), NI/slab (dashed curve), and total (dashed–dotted–dashed) energy in forward-propagating modes as a function of heliocentric distance. The quasi-2D forward-propagating energy decreases by about an order of magnitude within 2 $R_\odot$ and then decreases more gradually as $r^{-0.59}$. Note that the theoretical quasi-2D energies in backward-propagating modes $\langle z^{\infty -2}\rangle$ and forward-propagating modes $\langle z^{\infty +2}\rangle$ overlap each other because the quasi-2D turbulence is balanced from 1 to 100 $R_\odot$ (see Figure 3(d)). The energy in NI/slab forward-propagating modes increases to a peak value of $1.73 \times 10^4$ km$^2$ s$^{-2}$ from the coronal base and then decreases as $r^{-0.16}$. Similarly, the total energy in forward-propagating modes decreases quickly near the coronal base and then follows a power law of $r^{-0.48}$. The red diamonds denote the observed energy in forward-propagating modes, which exhibits a radial decay of $r^{-0.96}$. Although the comparison shows that the theoretical and observed energies in forward-propagating modes are in reasonable agreement, the theoretical result decreases more slowly than the observed result. The observed $\langle z^{+2}\rangle$ shows some scatter and is close to both the energies in the quasi-2D $\langle z^{\infty +2}\rangle$ and NI/slab forward-propagating modes $\langle z^{*+2}\rangle$, where the total component (dashed–dotted–dashed curve) is larger than the observed $\langle z^{+2}\rangle$.

The evolution of the fluctuating magnetic energy as a function of heliocentric distance is plotted in Figure 3(b). At the coronal base, the quasi-2D fluctuating magnetic energy (solid curve) is assumed to be $6.062 \times 10^9$ (nT)$^2$, the NI/slab fluctuating magnetic energy (dashed curve) is $5.77 \times 10^6$ (nT)$^2$, and the total fluctuating magnetic energy (dashed–dotted–dashed curve) is $6.068 \times 10^9$ (nT)$^2$. The quasi-2D fluctuating magnetic energy is about three orders of magnitude larger than the NI/slab fluctuating magnetic energy at the coronal base. The quasi-2D component decreases more rapidly than the slab component inside 2 $R_\odot$, after which it decreases as $r^{-2.72}$, the NI/slab fluctuating magnetic energy as $r^{-2.28}$, and the total energy as $r^{-2.68}$. The red diamonds denote the observed fluctuating magnetic energy as a function of heliocentric distance. A least-squares fit shows that the observed fluctuating magnetic energy decreases as $r^{-3.32}$ between $\sim$40 $R_\odot$ and $\sim$100 $R_\odot$. PSP observations are made when the solar wind flow is well aligned with the mean

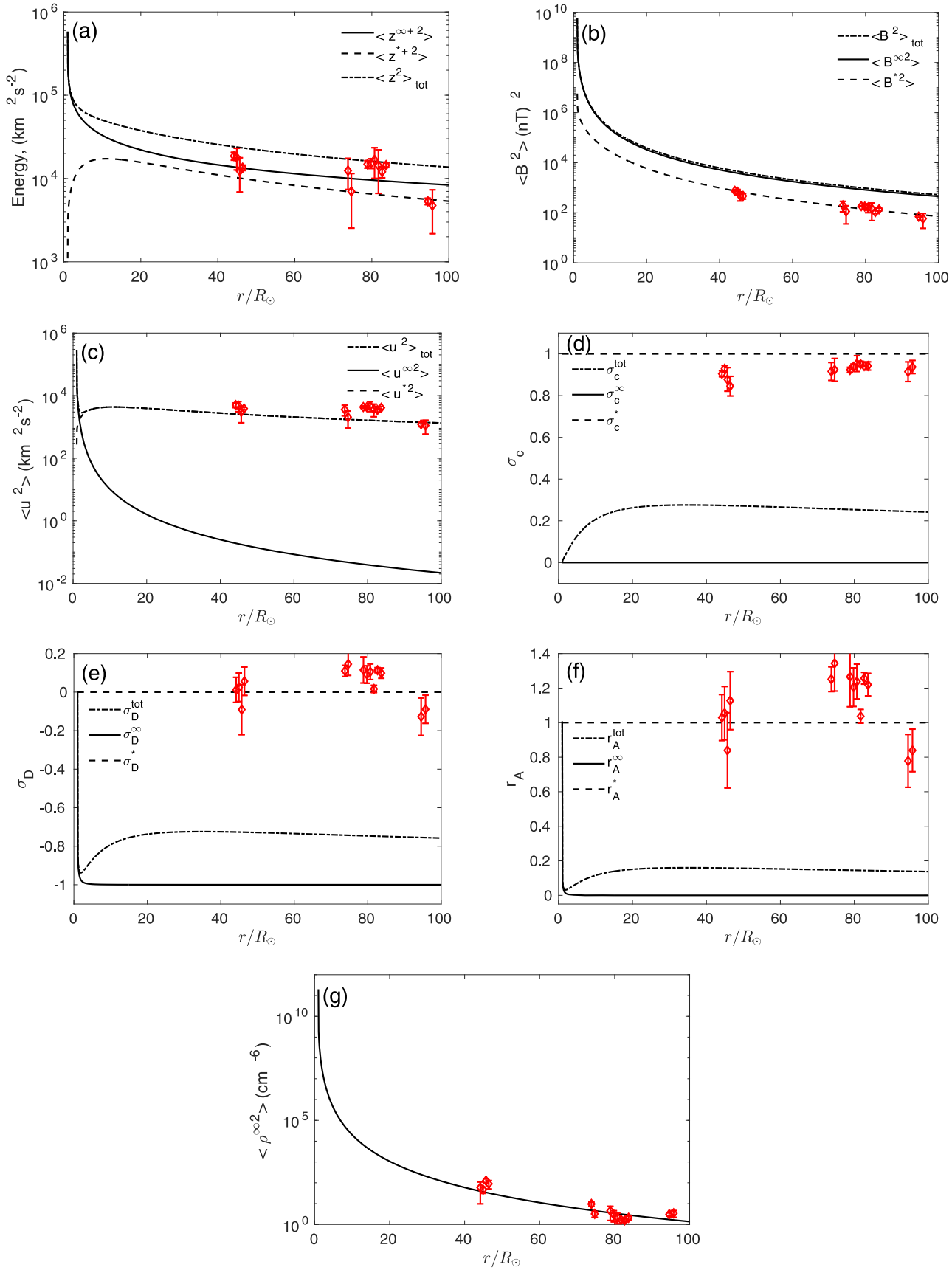


**Figure 3.** The panels show (a) the energy corresponding to forward-propagating modes; (b) the fluctuating magnetic energy; (c) the fluctuating kinetic energy; (d) the normalized cross-helicity; (e) the normalized residual energy; (f) the Alfvén ratio; and (g) the variance of the density fluctuations as a function of heliocentric distance. The solid curves denote the quasi-2D component, dashed curves the slab component, and dashed–dotted–dashed curves the total component. The red diamonds are the observed quantities with error bars.

magnetic field, and consequently only the slab-like fluctuations can be observed. Quasi-2D fluctuations cannot be directly measured. Hence, only the theoretical NI/slab model can be compared directly to PSP magnetic field measurements made in field-aligned flows (see Figure 1). Accordingly, in Figure 3(b), we show that the theoretical NI/slab curves overlay the PSP observations of $\langle B^2 \rangle$ well. The dominant magnetic energy density is contained in the quasi-2D modes, which cannot be observed by PSP.

The radial evolution of the fluctuating kinetic energy is shown in Figure 3(c). The quasi-2D fluctuating kinetic energy (solid curve) at the coronal base is assumed to be $2.91 \times 10^5$ km$^2$ s$^{-2}$, which decreases rapidly so that the quasi-2D fluctuating kinetic energy becomes negligible as distance increases. The NI/slab fluctuating kinetic energy (dashed curve) increases from the bottom of the solar corona, where the energy is about 275 km$^2$ s$^{-2}$, to $\sim 4.32 \times 10^3$ km$^2$ s$^{-2}$ at the Alfvén surface, and then decreases as $r^{-0.53}$. The total fluctuating kinetic energy (dashed–dotted–dashed curve) decreases initially and then follows a profile similar to that of the NI/slab fluctuating kinetic energy. The red diamonds with error bars are the observed turbulent kinetic energy as a function of distance, which follows a power law of $r^{-0.86}$. The radial profile of the NI/slab turbulent kinetic energy is similar to that of the observed turbulent kinetic energy.

As shown in Figure 1, the angle between the solar wind flow and the magnetic field is mostly around 0° or 180°. The red diamonds in Figure 3(d) denote the observed normalized cross-helicity with error bars. The average observed normalized cross-helicity is about 0.89. The solid, dashed, and dashed–dotted–dashed curves are the theoretical quasi-2D, NI/slab, and total normalized cross-helicity. The quasi-2D turbulence is assumed to be balanced (i.e., zero cross-helicity) at the coronal base and remains so until 100 $R_\odot$. In Zank et al. (2018), the balanced quasi-2D turbulence at the base of the solar corona becomes unbalanced with distance, because there are counterpropagating Alfvén waves that drive quasi-2D turbulence, but no such counterpropagating Alfvén waves exist in the current model. Additionally, the theoretical NI/slab normalized cross-helicity remains at 1 between 1 $R_\odot$ and 100 $R_\odot$ because there are no backward-propagating Alfvén waves in this model. The total normalized cross-helicity (dashed–dotted–dashed curve) increases initially and then decreases slightly with increasing heliocentric distance. As discussed above, because PSP observes primarily field-aligned flows, the measured cross-helicity refers only to NI/slab modes. Figure 3(d) shows that the theoretical slab and PSP-derived cross-helicities are consistent.

Similarly, the observed normalized residual energy with error bars shown in Figure 3(e) oscillates around the mean value of 0.0067 between 35.5 $R_\odot$ and 100 $R_\odot$. The quasi-2D normalized residual energy (solid curve) in the figure decreases rapidly to become $-1$ with increasing heliocentric distance. Hence, the quasi-2D turbulence evolves to become primarily quasi-2D fluctuating magnetic energy, that is, essentially small-scale magnetic islands or flux ropes. The theoretical NI/slab normalized residual energy (dashed curve) is zero between 1 $R_\odot$ and 100 $R_\odot$, similar to that observed (red diamonds) for the reasons discussed above. Figure 3(f) shows the Alfvén ratio as a function of heliocentric distance. The observed Alfvén ratio (red diamonds) oscillates around an average value of 1.0384. The theoretical NI/slab Alfvén ratio (dashed curve) and the observed Alfvén ratio show good agreement between 35.5 $R_\odot$ and 100 $R_\odot$. The consistency of the observed and theoretical normalized cross-helicity, normalized residual energy, Alfvén ratio, and the angle between the solar wind flow and the magnetic field suggests that the fast solar wind observed by PSP over the interval 35.5 $R_\odot$ to 100 $R_\odot$ supports our assumptions of setting $\sigma_c^* = 1$ or $\langle z^{*-2} \rangle = 0$ and $\sigma_D^* = 0$ or $E_D^* = 0$ in deriving turbulence transport model equations for the fast solar wind. Typically, such observations are used to argue that the solar wind is highly Alfvénic despite the observation of a nonadiabatic temperature profile (unidirectional Alfvén wave propagation $|\sigma_c| = 1$, $\sigma_D = 0$, does not support turbulence, and hence turbulent or dissipative heating is not possible) and often a Kolmogorov-like wavenumber spectrum $k_{||}^{-5/3}$ (Telloni et al. 2019; Zhao et al. 2020b; $k_{||}$ being the wavenumber parallel to the solar wind flow). Instead, our results demonstrate that the fast wind is dominated by quasi-2D turbulence that cannot be measured by PSP because the flow is highly field aligned. However, the slab component of the 2D + slab decomposition of NI MHD allows us to compare directly the slab predictions to PSP observations. As illustrated in Figure 3 (and 2), the comparison of the theory and observation is very good.

The comparison between the theoretical and observed variances of the density fluctuations as a function of heliocentric distance is shown in Figure 3(g). The theoretical density variance at the base of the solar corona is assumed to be $2 \times 10^{12}$ cm$^{-6}$, which decreases by about three orders of magnitude within 2 $R_\odot$ and then decreases more slowly and monotonically as distance increases. The red diamonds with error bars denote the observed density variance measured by the PSP. The observations follow a radial profile of $\sim r^{-6.1}$. A similar analysis by Adhikari et al. (2020) found that the radial profile of the variance of the density fluctuations in the slow wind between 35.5 $R_\odot$ and 131.64 $R_\odot$ is about $r^{-2.98}$. These two results clearly show the differences in the density variance in the fast and slow solar winds. The theoretical density variance decreases and is consistent with that observed between 35.5 $R_\odot$ and 100 $R_\odot$.

Figure 4(a) describes the evolution of the correlation function as a function of heliocentric distance. The solid and dashed curves correspond to the correlation function for the quasi-2D forward- and backward-propagating modes, respectively, and the dashed–dotted–dashed curve corresponds to the correlation function of the residual energy. The correlation function decreases quickly in the vicinity of the coronal base and then remains approximately constant until 100 $R_\odot$, where $L_\infty^+$ and $L_\infty^-$ show the same radial profiles with increasing distance. In the figure, $L_\infty^+$ and $L_\infty^-$ overlap, so they do not appear to be distinct. The rapid decrease of $L_\infty^+$ and $L_\infty^-$ leads to a stronger nonlinear decay term near the coronal base, which results in the rapid dissipation of the turbulent energy and leads to the rapid increase in the temperature of the coronal plasma.

Figure 4(b) plots the correlation lengths of the Elsässer energies and the residual energy as a function of heliocentric distance. The correlation lengths corresponding to quasi-2D forward- and backward-propagating modes (solid and dashed curves, respectively) show the same radial profiles and increase as distance increases. The dashed–dotted–dashed red curve denotes the correlation length for the quasi-2D residual energy, which increases more rapidly than the correlation lengths of the forward- and backward-propagating modes. The dashed–dotted–dashed black curve corresponds to the correlation length of NI/slab outward-propagating modes. The red

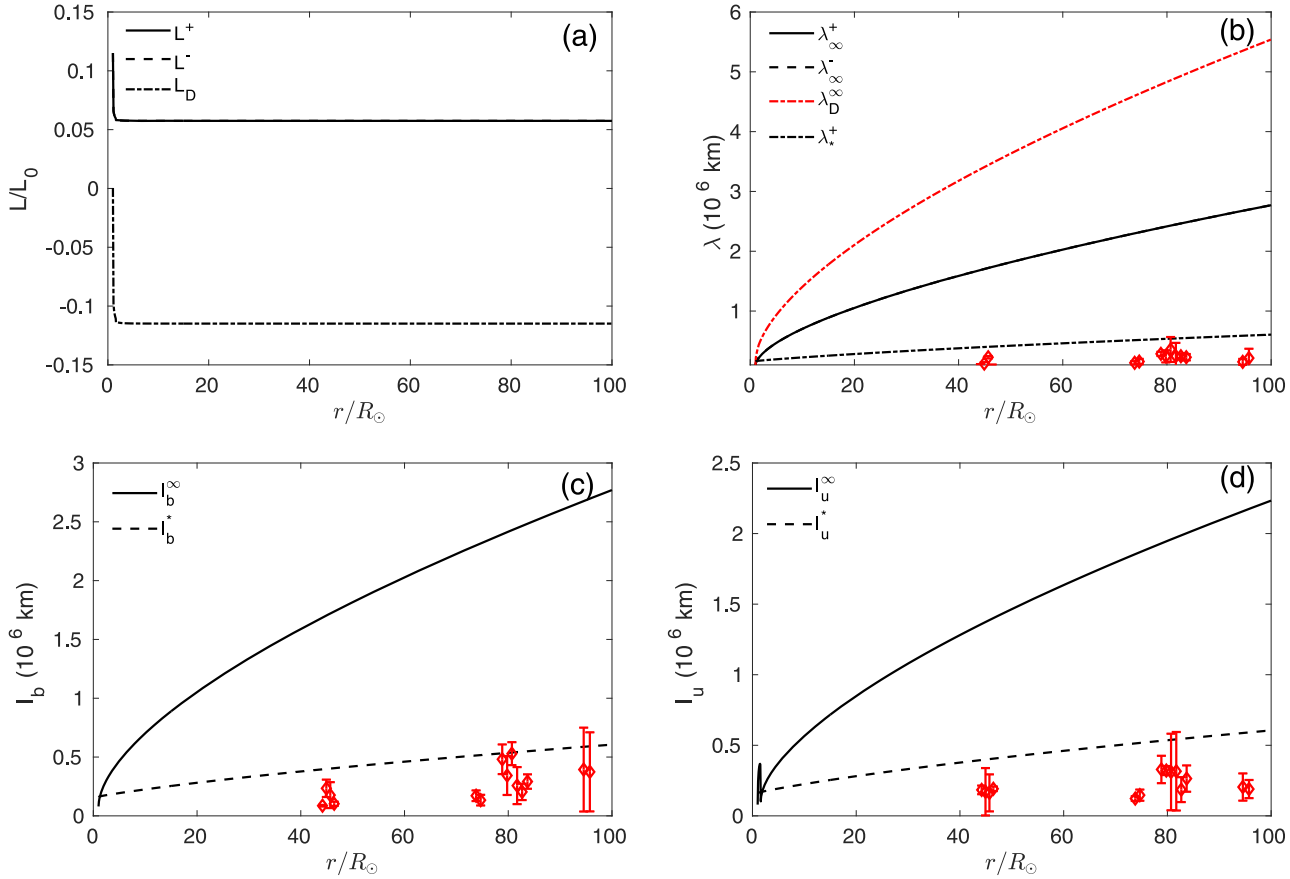


**Figure 4.** The panels show (a) the correlation functions, (b) the correlation lengths, (c) the correlation lengths of magnetic field fluctuations, and (d) the correlation lengths of velocity fluctuations as a function of heliocentric distance. The conventions for the figure are the same as used in Figure 3. The red diamonds are observed correlation lengths with error bars.

diamonds with error bars are the observed correlation lengths of forward-propagating modes. The observed correlation length corresponding to forward-propagating modes is smaller than the theoretical NI/slab correlation length (dashed–dotted–dashed curve), which may be due to the large correlation length used at the coronal base.

Figure 4(c) shows the correlation length of magnetic field fluctuations as a function of heliocentric distance. Similar to the correlation lengths of the Elsässer variables, the correlation length for quasi-2D magnetic field fluctuations (solid curve) increases more rapidly than the correlation length of slab magnetic field fluctuations (dashed curve). The correlation length corresponding to NI/slab magnetic field fluctuations is larger than the observed correlation length of magnetic field fluctuations within $\sim$78 $R_\odot$, and they are close between $\sim$80 $R_\odot$ and $\sim$100 $R_\odot$.

The correlation length for the fluctuating kinetic energy is plotted in Figure 4(d). Compared with the quasi-2D correlation length (solid curve) for the fluctuating kinetic energy, the correlation length (dashed curve) of the NI/slab fluctuating kinetic energy is close to the observed correlation length (red diamonds), although a little larger in general. The correlation length (solid curve) for the quasi-2D fluctuating kinetic energy is larger and increases more rapidly than the correlation length of the NI/slab fluctuating kinetic energy. These results show that in the fast solar wind, the correlation length of the quasi-2D turbulence is larger than the correlation length of the NI/slab turbulence, which is different from that in the slow solar wind. Adhikari et al. (2020) found that the correlation length of NI/slab turbulence (in the slow solar wind) is larger than that of quasi-2D turbulence from 35.5 $R_\odot$ to 131.64 $R_\odot$.

## 4. Discussion and Conclusions

We developed a self-consistent nearly incompressible magnetohydrodynamic (NI MHD) turbulence-driven solar wind model for open-field solar coronal holes in which the solar wind flow is aligned with the magnetic field. By assuming equipartition between the NI/slab fluctuating kinetic and magnetic energies and that the normalized NI/slab cross-helicity is $|\sigma_c^*| = 1$, we derived coupled NI MHD quasi-2D and NI/slab turbulence transport model equations. Unlike the high plasma beta turbulence transport model equations (Zank et al. 2012), these assumptions do not eliminate the nonlinear term of the NI/slab turbulence transport model equations, indicating that NI/slab turbulence does not turn off (Adhikari et al. 2019b) at the Alfvén surface. Recent analysis of both WIND and PSP data sets for highly aligned flows find that unidirectional Alfvén waves exhibit a Kolmogorov-type of power law (Telloni et al. 2019; Zhao et al. 2020b), which is consistent with the spectral analysis of NI MHD by Zank et al. (2020). The coupled quasi-2D and NI/slab turbulence transport model equations derived here incorporate unidirectional Alfvén waves in a 2D + slab NI MHD framework (Telloni et al. 2019;

Zank et al. 2020; Zhao et al. 2020b) and correspond to a small plasma $\beta_p \ll 1$ or $\sim 1$ regime (Zank et al. 2017). In our model, the dissipation of quasi-2D turbulence mainly heats the coronal plasma above the photosphere (Zank et al. 2018), and it is closely related to the idea of random twisting and braiding of magnetic field lines, which dissipates magnetic energy in the form of nanoflares above the photosphere (Parker 1972, 1988; Fisk et al. 1999; Rappazzo & Parker 2013; Zank et al. 2018).

As discussed in Zank et al. (2020), the unidirectional propagating Alfvén waves interact passively with the quasi-2D turbulence, which results in a Kolmogorov-like $k_{||}^{-5/3}$ spectrum. The absence of slab "turbulence" is a consequence of the Alfvén timescale $\tau_A \sim \lambda_A / V_{A0}$ greatly exceeding the nonlinear timescale $\tau_{nl}^{\infty} \sim \lambda_{\perp}^{\infty} / \langle z^{\infty 2} \rangle$, where $\lambda_A$ and $\lambda_{\perp}^{\infty}$ are the Alfvénic and quasi-2D correlation lengths. When $\tau_A \gg \tau_{nl}^{\infty}$, Zank et al. (2020) show that the turbulence is strong and dominated by nonlinear interactions and that, other than passively responding to the quasi-2D fluctuations, Alfvén waves propagate unidirectionally in the turbulent flow.

We extended the Zank et al. (2018) model by coupling the NI MHD quasi-2D and NI/slab turbulence transport equations with the solar wind equations. Here, we solved the coupled solar wind equations and the nearly incompressible turbulence transport model equations simultaneously from the base of the solar corona to 100 solar radii, in which the continuity, momentum, and thermal temperature equations provide the background profiles for the solar wind density and speed. We compared our theoretical solutions with the fast solar wind measured by PSP on its first orbit in the outbound direction. We summarize our findings as follows:

1. The solar wind speed increases rapidly from a subsonic state to a supersonic state within a few solar radii, consistent with observations reported by Telloni et al. (2007), and then monotonically increases as a function of heliocentric distance. The theoretical solar wind speed is similar to the fast solar wind observed by PSP between 35.5 $R_{\odot}$ and 100 $R_{\odot}$.
2. The temperature of the coronal plasma becomes of the order of $10^6$ K within a few solar radii. The theoretical solar wind proton temperature is in reasonable agreement with the observed proton temperature between 35.5 $R_{\odot}$ and 100 $R_{\odot}$.
3. The solar wind density decreases rapidly near the coronal base due to the rapid increase in the solar wind speed. The radial profile of the theoretical solar wind density is similar to the observed solar wind density between 35.5 $R_{\odot}$ and 100 $R_{\odot}$.
4. The heating rate of quasi-2D turbulence is $\sim 10^3$ times higher than that of the NI/slab turbulence, indicating that the dissipation of quasi-2D turbulence near the coronal base is sufficient to heat the coronal plasma up to millions of degrees kelvin, thus driving the solar wind from a subsonic to a supersonic state.
5. The Alfvén velocity increases from 900 km s$^{-1}$ to 2.79 $\times$ $10^3$ km s$^{-1}$ within 2 $R_{\odot}$ and then decreases with increasing heliocentric distance. The Alfvén surface forms at a heliocentric distance of $\sim 11.7$ $R_{\odot}$, and a sonic surface forms at $\sim 1.78$ $R_{\odot}$.
6. The majority quasi-2D energy in forward-propagating modes decreases rapidly near the coronal base, and then gradually decreases as a function of heliocentric distance. The slab energy in forward-propagating modes increases to a peak value of 1.73 $\times$ $10^4$ km$^2$ s$^{-2}$ and then decreases with distance. The theoretical quasi-2D and NI/slab energies in forward-propagating modes are comparable to the energy observed in forward-propagating modes.
7. The quasi-2D, NI/slab, and total fluctuating magnetic energy decreases as distance increases. The observed fluctuating magnetic energy and the NI/slab fluctuating magnetic energy show good agreement between 35.5 $R_{\odot}$ and 100 $R_{\odot}$.
8. The quasi-2D fluctuating kinetic energy is large at the coronal base compared to the slab fluctuating kinetic energy. However, the quasi-2D fluctuating kinetic energy decreases rapidly with increasing heliocentric distance, whereas the NI/slab fluctuating kinetic energy increases initially to a peak value of 4.32 $\times$ $10^3$ km$^2$ s$^{-2}$ and then decreases with increasing distance. The radial profile of the slab fluctuating kinetic energy is similar to the observed fluctuating kinetic energy between 35.5 $R_{\odot}$ and 100 $R_{\odot}$.
9. The average observed normalized cross-helicity, residual energy, and Alfvén ratio are close to 0.89, 0.0067, and 1.0384 in the fast solar wind and are similar to the theoretical NI/slab quantities.
10. The theoretical quasi-2D and NI/slab correlation lengths increase as a function of heliocentric distance. The correlation length for quasi-2D turbulence increases faster than the correlation length of slab turbulence. The observed correlation length is smaller than the NI/slab correlation length with increasing heliocentric distance.
11. The variance of the density fluctuations decreases as a function of heliocentric distance, and the theoretical and observed variances show good agreement between 35.5 $R_{\odot}$ and 100 $R_{\odot}$.

The nonadiabatic temperature profile observed in a highly Alfvénic solar wind flow (i.e., unidirectional Alfvén wave propagation $|\sigma_c| = 1$ and $\sigma_D = 0$) shows that turbulent heating of the solar wind flow is possible. Our results show that the fast wind is dominated by quasi-2D turbulence that cannot be measured by PSP because the flow is highly field aligned (Telloni et al. 2019; Zank et al. 2020; Zhao et al. 2020b). However, the slab component of the 2D + slab decomposition of NI MHD can be compared directly with observations. The results show that the theoretical NI/slab turbulent energy and correlation length are similar to the PSP measurements of the fast solar wind flow.

We acknowledge the partial support of a Parker Solar Probe contract SV4-84017, an NSF-DOE grant PHY-1707247, and an NSF EPSCoR RII-Track-1 cooperative agreement OIA-1655280. The Parker Solar Probe (PSP) magnetometer and plasma data were obtained from the NASA CDAWeb website.

## Appendix A
## NI/Slab Turbulence Transport Equations

To derive transport equations for $\langle z^{*\pm 2} \rangle$, we start with Equation (83) of Zank et al. (2017), which is the transport equation for the minority Elsässer variables $z^{*\pm}$ for an

inhomogeneous $\beta_p \sim 1$ plasma:

$$\frac{\partial z^{*\pm}}{\partial t} + (\boldsymbol{U} \mp \boldsymbol{V}_A)\cdot\nabla z^{*\pm} + z^{\infty\mp}\cdot\nabla z^{*\pm} + z^{*\mp}\cdot\nabla z^{\infty\pm} + z^{*\mp}\cdot\nabla z^{*\pm} + \frac{1}{4}(z^{*\pm} - z^{*\mp})\nabla\cdot\boldsymbol{U} + z^{*\mp}\cdot\nabla(\boldsymbol{U}\pm\boldsymbol{V}_A) \pm \frac{1}{2}\frac{1}{\rho}z^{*\mp}\cdot\nabla\rho\boldsymbol{V}_A - \frac{1}{4}(z^{*+} - z^{*-})\frac{1}{\rho}\boldsymbol{V}_A\cdot\nabla\rho \pm \frac{1}{4}(z^{\infty+} - z^{\infty-})\frac{1}{\rho}z^{*\mp}\cdot\nabla\rho \mp \frac{1}{4}(z^{*+} - z^{*-}) \times \frac{1}{\rho}z^{\infty\pm}\cdot\nabla\rho \mp \frac{1}{2}(z^{*+} - z^{*-})\cdot\nabla\boldsymbol{U} = -\frac{1}{\rho}\nabla(P^* + \boldsymbol{B}^*\cdot\boldsymbol{B}/\mu_0 + \boldsymbol{B}^*\cdot\boldsymbol{B}^\infty/\mu_0), \quad (15)$$

where $z^{*\pm} = \boldsymbol{u}^* \pm \boldsymbol{b}^*/\sqrt{\mu_0\rho}$, and $z^{*+}$ and $z^{*-}$ indicate forward- and backward-propagating modes, respectively. Equation (15) shows that the higher-order, nearly incompressible Elsässer variables couple with the leading-order core $z^{\infty\pm}$ variables in a passive scalar sense, so the primary dissipation mechanism for $z^{*\pm}$ is due to mixing rather than nonlinearity. Equation (15) contains three timescales: the Alfvén timescale $\tau_A = \lambda_A/V_{A0}$, the quasi-2D nonlinear timescale $\tau_\pm^\infty = \lambda_\infty^\pm/\langle z^{\infty\mp 2}\rangle$, and the NI nonlinear timescale $\tau_\pm^* = \lambda_*^\pm/\langle z^{*\mp 2}\rangle$. The quasi-2D and NI nonlinear timescales satisfy the ordering of $\lambda_\infty^\pm/\langle z^{\infty\mp 2}\rangle \gg \lambda_*^\pm/\langle z^{*\mp 2}\rangle$ (see Zank et al. 2020 for further discussion). Taking a dot product between $z^{*\pm}$ and Equation (15), we find the transport equations for $\langle z^{*\pm 2}\rangle$ are (Zank et al. 2017)

$$\frac{\partial\langle z^{*+2}\rangle}{\partial t} + (\boldsymbol{U} - \boldsymbol{V}_A)\cdot\nabla\langle z^{*+2}\rangle + \frac{1}{2}\langle z^{*+2}\rangle\nabla\cdot\boldsymbol{U} - \frac{1}{2}E_D^*\nabla\cdot\boldsymbol{U} + 2bE_D^*\Big(\nabla\cdot(\boldsymbol{U} + \boldsymbol{V}_A) - s_is_j\Big(\frac{\partial U_i}{\partial x_j} + \frac{\partial V_{Ai}^{sw}}{\partial x_j}\Big)\Big) + \frac{b}{\rho}E_D^*\Big(\boldsymbol{V}_A\cdot\nabla\rho - s_is_jV_{Ai}\frac{\partial\rho}{\partial x_j}\Big) - \frac{1}{2}(\langle z^{*+2}\rangle - E_D^*)\frac{1}{\rho}\boldsymbol{V}_A\cdot\nabla\rho + \frac{1}{2}\frac{1}{\rho}(\langle z^{*+}\cdot z^{\infty+}\rangle - \langle z^{*+}\cdot z^{\infty-}\rangle)z^{*-}\cdot\nabla\rho - \frac{1}{2}\frac{1}{\rho}(\langle z^{*+2}\rangle - E_D^*)\langle z^{\infty+2}\rangle^{1/2}\hat{n}\cdot\nabla\rho - b(\langle z^{*+2}\rangle - E_D^*)\Big(\nabla\cdot\boldsymbol{U} - s_is_j\frac{\partial U_i}{\partial x_j}\Big) = -2\frac{\langle z^{*+2}\rangle\langle z^{\infty-2}\rangle^{1/2}}{\lambda_\infty^+} - 2\frac{\langle z^{*+2}\rangle\langle z^{*-2}\rangle^{1/2}}{\lambda_*^+} - 2\frac{\langle z^{*+}\cdot z^{\infty+}\rangle\langle z^{*-2}\rangle^{1/2}}{\lambda_*^+}; \quad (16)$$

$$\frac{\partial\langle z^{*-2}\rangle}{\partial t} + (\boldsymbol{U} + \boldsymbol{V}_A)\cdot\nabla\langle z^{*-2}\rangle + \frac{1}{2}\langle z^{*-2}\rangle\nabla\cdot\boldsymbol{U} - \frac{1}{2}E_D^*\nabla\cdot\boldsymbol{U} + 2bE_D^*\Big(\nabla\cdot(\boldsymbol{U} - \boldsymbol{V}_A) - s_is_j\Big(\frac{\partial U_i}{\partial x_j} - \frac{\partial V_{Ai}}{\partial x_j}\Big)\Big) - \frac{b}{\rho}E_D^*\Big(\boldsymbol{V}_A\cdot\nabla\rho - s_is_jV_{Ai}\frac{\partial\rho}{\partial x_j}\Big) + \frac{1}{2}(\langle z^{*-2}\rangle - E_D^*)\frac{1}{\rho}\boldsymbol{V}_A\cdot\nabla\rho - \frac{1}{2}\frac{1}{\rho}(\langle z^{*-}\cdot z^{\infty+}\rangle - \langle z^{*-}\cdot z^{\infty-}\rangle)z^{*+}\cdot\nabla\rho - \frac{1}{2}\frac{1}{\rho}(\langle z^{*-2}\rangle - E_D^*)\langle z^{\infty-2}\rangle^{1/2}\hat{n}\cdot\nabla\rho - b(\langle z^{*-2}\rangle - E_D^*)\Big(\nabla\cdot\boldsymbol{U} - s_is_j\frac{\partial U_i}{\partial x_j}\Big) = -2\frac{\langle z^{*-2}\rangle\langle z^{\infty+2}\rangle^{1/2}}{\lambda_\infty^-} - 2\frac{\langle z^{*-2}\rangle\langle z^{*+2}\rangle^{1/2}}{\lambda_*^-} - 2\frac{\langle z^{*-}\cdot z^{\infty-}\rangle\langle z^{*+2}\rangle^{1/2}}{\lambda_*^-}, \quad (17)$$

where we approximate $z^{\infty\pm} \simeq \langle z^{\infty\pm 2}\rangle^{1/2}\hat{n}$ ($\hat{n}$ is orthogonal to the large-scale magnetic field $\boldsymbol{B}_0$), and $E_D^* = \langle z^{*+}\cdot z^{*-}\rangle$ is the residual energy. In the derivation of Equations (16) and (17), we express a covariance with zero lag as $Q_{ij}(0) = b(\delta_{ij} - s_is_j)$ (Batchelor 1953; Zank et al. 2012, 2017).

We now impose a condition of Alfvénicity $E_D^* = 0$ or $\sigma_D^* = 0$ and $E_C^* = 1$ or $\sigma_c^* = 1$ in Equations (16) and (17). The parameter $\sigma_D^*$ is the normalized residual energy, $\sigma_c^*$ is the normalized cross-helicity, and $E_C^*$ is the cross-helicity. These are the measures of Alfvénicity where the fluctuating kinetic and the fluctuating magnetic field are almost aligned so that $z^{*-} \to 0$ or $\langle z^{*-2}\rangle \to 0$, indicating that the backward modes are approximately zero. Also, near the Sun where the magnetic field is almost radial, $\hat{n}\cdot\nabla\rho = 0$. Under these conditions, Equation (16) reduces to

$$\frac{\partial\langle z^{*+2}\rangle}{\partial t} + (\boldsymbol{U} - \boldsymbol{V}_A)\cdot\nabla\langle z^{*+2}\rangle + \frac{1}{2}\langle z^{*+2}\rangle\nabla\cdot\boldsymbol{U} - \frac{1}{2}\langle z^{*+2}\rangle\Big(\frac{1}{\rho}\boldsymbol{V}_A\cdot\nabla\rho + 2b\Big(\nabla\cdot\boldsymbol{U} - s_is_j\frac{\partial U_i}{\partial x_j}\Big)\Big) = -2\frac{\langle z^{*+2}\rangle\langle z^{\infty-2}\rangle^{1/2}}{\lambda_\infty^+}, \quad (18)$$

and Equation (17) becomes

$$0 = 0. \quad (19)$$

Equations (18) and (19) show that the transport equation for the backward-propagating modes for slab turbulence vanishes, so we only need to solve the transport equation for the outward-propagating modes.

We derive the transport equation for the correlation function $L_*^\pm\Big(=\int\langle z^{*\pm}\cdot z^{*\pm'}\rangle dr \equiv \langle z^{*\pm}\cdot z^{*\pm}\rangle\lambda_*^\pm\Big)$ corresponding to forward/backward-propagating modes for the Alfvénic (NI/slab)

turbulence. The parameters $z^{*\pm\prime} \equiv z^{*\pm}(\boldsymbol{x}+\boldsymbol{r})$ denote the lagged Elsässer variables at a location $r$ from $x$. We start from Equation (87) of Zank et al. (2017):

$$\frac{\partial L_*^{\pm}}{\partial t} + (\boldsymbol{U} \mp \boldsymbol{V}_A)\cdot\nabla L_*^{\pm} + \frac{1}{2}L_*^{\pm}\nabla\cdot\boldsymbol{U} + (b-\frac{1}{4})L_D^*\nabla\cdot\boldsymbol{U} - bL_D^* s_i s_j \frac{\partial U_i}{\partial x_j} \pm bL_D^* \left(\nabla\cdot\boldsymbol{V}_A + \frac{1}{2}\frac{1}{\rho}\boldsymbol{V}_A\cdot\nabla\rho - s_i s_j\frac{\partial V_{Ai}}{\partial x_j} - \frac{1}{2}s_i s_j V_{Ai}\frac{1}{\rho}\frac{\partial\rho}{\partial x_j}\right) \mp \frac{1}{2}\left(L_*^{\pm} - \frac{L_D^*}{2}\right)\left[\frac{1}{\rho}\boldsymbol{V}_A\cdot\nabla\rho_{sw} \pm \frac{1}{\rho}\langle z^{\infty\pm 2}\rangle^{1/2}\hat{n}\cdot\nabla\rho \pm 2b\left(\nabla\cdot\boldsymbol{U} - s_i s_j\frac{\partial U_i}{\partial x_j}\right)\right] = 0, \quad (20)$$

where $L_D^* = \int \langle \boldsymbol{z}^{*+}\cdot\boldsymbol{z}^{*-\prime} + \boldsymbol{z}^{*+\prime}\cdot\boldsymbol{z}^{*-}\rangle dr \equiv E_D^*\lambda_D^*$ is the correlation function corresponding to the NI/slab residual energy. Since $E_D^* = 0$ implies that $L_D^* = 0$, $\langle z^{*-2}\rangle = 0$ implies that $L_*^- = 0$, and $\hat{n}\cdot\nabla\rho = 0$ for the radial magnetic field, Equation (20) reduces to

$$\frac{\partial L_*^{+}}{\partial t} + (\boldsymbol{U} - \boldsymbol{V}_A)\cdot\nabla L_*^{+} + \frac{1}{2}L_*^{+}\nabla\cdot\boldsymbol{U} - \frac{1}{2}L_*^{+}\left[\frac{1}{\rho}\boldsymbol{V}_A\cdot\nabla\rho + 2b\left(\nabla\cdot\boldsymbol{U} - s_i s_j\frac{\partial U_i}{\partial x_j}\right)\right] = 0 \quad (21)$$

for the $L_*^+$ and $0 = 0$ for the $L_*^-$. Equation (21) shows that we only need to solve the transport equation for the correlation function corresponding to NI/slab outward-propagating modes. Equations (18) and (21) describe the evolution of unidirectional propagating modes and the corresponding correlation function.

## Appendix B
## Data Analysis

We select four unperturbed plasma intervals in the fast solar wind flow as measured by the SWEAP (Kasper et al. 2016) and FIELDs (Bale et al. 2016) instruments on PSP. The start and end times (DOY:HR:MN) of the intervals are (312:13:0.378–313:8:46.54), (318:1:56.62–319:5:54.51), (319:21:25.64–321:7:59.89), and (323:7:7.16—324.0.46:27.35). These intervals are approximately one-day intervals during which the solar wind speed does not experience any sudden changes. We derive turbulent quantities using the observed T and N components of the solar wind speed and magnetic field and the solar wind density (Borovsky 2016; Adhikari et al. 2017; Zhao et al. 2018a). We consider first a time interval of 4 hr and calculate the fluctuating velocity and the magnetic field using $\boldsymbol{u} = \boldsymbol{U} - \langle\boldsymbol{U}\rangle$ and $\boldsymbol{b} = \boldsymbol{B} - \langle\boldsymbol{B}\rangle$, where $\langle\boldsymbol{U}\rangle$ and $\langle\boldsymbol{B}\rangle$ are the mean solar wind speed and the magnetic field. Then we calculate the Elsässer variable $\boldsymbol{z}^{\pm} = \boldsymbol{u} \pm \boldsymbol{b}/\sqrt{\mu_0\rho_0}$, where $\rho_0$ is the mean solar wind mass density, and $\mu_0$ is the magnetic permeability. We calculate the variance of the $\boldsymbol{u}$, $\boldsymbol{b}$, and Elsässer variables, which describe the fluctuating kinetic energy, fluctuating magnetic energy, and the Elsässer energies, respectively (Zank et al. 1996; Adhikari et al. 2015). We also calculate the variance of the solar wind density in a time interval of 4 hr. We derive the normalized residual energy $\sigma_D$, the normalized cross-helicity $\sigma_c$, and the Alfvén ratio $r_A$ from

$$\sigma_D = \frac{\langle u^2\rangle - \langle b^2/\mu_0\rho_0\rangle}{\langle u^2\rangle + \langle b^2/\mu_0\rho_0\rangle}; \quad \sigma_c = \frac{\langle z^{+2}\rangle - \langle z^{-2}\rangle}{\langle z^{+2}\rangle + \langle z^{-2}\rangle};$$
$$r_A = \frac{\langle u^2\rangle}{\langle b^2/\mu_0\rho_0\rangle}.$$

Similarly, we calculate the correlation length corresponding to forward-propagating modes $\lambda^+$, the correlation length of the velocity fluctuations $l_u$, and the correlation length of the magnetic field fluctuations. For this, we calculate the autocorrelation function as a function of lag *time* (Adhikari et al. 2015). Using Taylor's hypothesis, we convert lag *time* to lag *distance*. The correlation length corresponds to lag *distance* at which the autocorrelation is 1/e of the maximum value (see also Shiota et al. 2017).

Finally, we smooth the data, in which we apply a criterion that the mean square fluctuations of the velocity, magnetic field, solar wind density, and solar wind temperature should be smaller than the square of the corresponding mean fields, which avoids data associated with shocks and other structures embedded in the solar wind. The data that do not satisfy this criterion are neglected, and then the remaining values are averaged. Because of the different lengths of data points in the interval, we smooth the data in different ways. The first and second intervals are smoothed by 30 data points, the third interval is smoothed by 15 data points, and the fourth interval is smoothed by six data points.

## ORCID iDs

L. Adhikari https://orcid.org/0000-0003-1549-5256
G. P. Zank https://orcid.org/0000-0002-4642-6192
L.-L. Zhao https://orcid.org/0000-0002-4299-0490

## References

Abramenko, V. I., Zank, G. P., Dosch, A., et al. 2013, ApJ, 773, 167
Adhikari, L., Khabarova, O., Zank, G. P., & Zhao, L. L. 2019a, ApJ, 873, 72
Adhikari, L., Zank, G. P., Bruno, R., et al. 2015, ApJ, 805, 63
Adhikari, L., Zank, G. P., Hunana, P., et al. 2017, ApJ, 841, 85
Adhikari, L., Zank, G. P., & Zhao, L. L. 2019b, ApJ, 876, 26
Adhikari, L., Zank, G. P., & Zhao, L. L. 2019c, JPhCS, 1332, 012001
Adhikari, L., Zank, G. P., Zhao, L. L., et al. 2020, ApJS, 246, 38
Badman, S. T., Bale, S. D., Martínez Oliveros, J. C., et al. 2020, ApJS, 246, 23
Bale, S. D., Goetz, K., Harvey, P. R., et al. 2016, SSRv, 204, 49
Bandyopadhyay, R., Goldstein, M. L., Maruca, B. A., et al. 2020, ApJS, 246, 48
Batchelor, G. K. 1953, The Theory of Homogeneous Turbulence (Cambridge: Cambridge Univ. Press)
Borovsky, J. E. 2016, JGRA, 121, 5055
Chandran, B. D. G., & Hollweg, J. V. 2009, ApJ, 707, 1659
Chandran, B. D. G., Li, B., Rogers, B. N., Quataert, E., & Germaschewski, K. 2010, ApJ, 720, 503
Chen, C. H. K., Bale, S. D., Bonnell, J. W., et al. 2020, ApJS, 246, 53
Cirtain, J. W., Golub, L., Lundquist, L., et al. 2007, Sci, 318, 1580
Cranmer, S. R., & van Ballegooijen, A. A. 2010, ApJ, 720, 824
Cranmer, S. R., van Ballegooijen, A. A., & Edgar, R. J. 2007, ApJS, 171, 520
Cranmer, S. R., van Ballegooijen, A. A., & Woolsey, L. N. 2013, ApJ, 767, 125
De Pontieu, B., McIntosh, S. W., Carlsson, M., et al. 2007, Sci, 318, 1574
Dmitruk, P., Matthaeus, W. H., Milano, L. J., et al. 2002, ApJ, 575, 571
Dmitruk, P., Milano, L. J., & Matthaeus, W. H. 2001, ApJ, 548, 482
Erdélyi, R., & Fedun, V. 2007, Sci, 318, 1572
Fisk, L. A., Schwadron, N. A., & Zurbuchen, T. H. 1999, JGR, 104, 19765
Fox, N. J., Velli, M. C., Bale, S. D., et al. 2016, SSRv, 204, 7
Goldreich, P., & Sridhar, S. 1995, ApJ, 438, 763

Habbal, S. R., Esser, R., Guhathakurta, M., & Fisher, R. R. 1995, GeoRL, 22, 1465
Hollweg, J. V. 1986, JGR, 91, 4111
Holzer, T. E., & Axford, W. I. 1970, ARA&A, 8, 31
Hunana, P., & Zank, G. P. 2010, ApJ, 718, 148
Kasper, J. C., Abiad, R., Austin, G., et al. 2016, SSRv, 204, 131
Kopp, R. A., & Holzer, T. E. 1976, SoPh, 49, 43
Kuridze, D., Morton, R. J., Erdélyi, R., et al. 2012, ApJ, 750, 51
Leer, E., Holzer, T. E., & Fla, T. 1982, SSRv, 33, 161
Mathioudakis, M., Jess, D. B., & Erdélyi, R. 2013, SSRv, 175, 1
Matthaeus, W. H., Zank, G. P., Oughton, S., Mullan, D. J., & Dmitruk, P. 1999, ApJL, 523, L93
McComb, W. D. 1995, RPPh, 58, 1117
McKenzie, J. F., Banaszkiewicz, M., & Axford, W. I. 1995, A&A, 303, L45
Montagud-Camps, V., Grappin, R., & Verdini, A. 2018, ApJ, 853, 153
Moore, R. L., Falconer, D. A., Porter, J. G., & Suess, S. T. 1999, ApJ, 526, 505
Moore, R. L., Sterling, A. C., & Falconer, D. A. 2015, ApJ, 806, 11
Morton, R. J., Tomczyk, S., & Pinto, R. F. 2016, ApJ, 828, 89
Okamoto, T. J., & De Pontieu, B. 2011, ApJL, 736, L24
Oughton, S., Matthaeus, W. H., Dmitruk, P., et al. 2001, ApJ, 551, 565
Parashar, T. N., Goldstein, M. L., Maruca, B. A., et al. 2020, ApJS, 246, 58
Parker, E. N. 1958, ApJ, 128, 664
Parker, E. N. 1972, ApJ, 174, 499
Parker, E. N. 1988, ApJ, 330, 474
Parker, E. N. 1994, in Proc. 7th European Meeting on Solar Physics, Advances in Solar Physics, ed. G. Belvedere, M. Rodonò, & G. M. Simnett (Berlin: Springer), 1
Rappazzo, A. F., Matthaeus, W. H., Ruffolo, D., Servidio, S., & Velli, M. 2012, ApJL, 758, L14
Rappazzo, A. F., & Parker, E. N. 2013, ApJL, 773, L2
Shebalin, J. V., Matthaeus, W. H., & Montgomery, D. 1983, JPlPh, 29, 525
Shiota, D., Zank, G. P., Adhikari, L., et al. 2017, ApJ, 837, 75
Stansby, D., Horbury, T. S., & Matteini, L. 2019, MNRAS, 482, 1706
Suzuki, T. K., & Inutsuka, S.-i 2005, ApJL, 632, L49
Telloni, D., Antonucci, E., & Dodero, M. A. 2007, A&A, 476, 1341
Telloni, D., Carbone, F., Bruno, R., et al. 2019, ApJ, 887, 160
Title, A. M., & Schrijver, C. J. 1998, in ASP Conf. Ser. 154, Cool Stars, Stellar Systems, and the Sun, ed. R. A. Donahue & J. A. Bookbinder (San Francisco, CA: ASP), 345
Tomczyk, S., & McIntosh, S. W. 2009, ApJ, 697, 1384
Tomczyk, S., McIntosh, S. W., Keil, S. L., et al. 2007, Sci, 317, 1192
van Ballegooijen, A. A., & Asgari-Targhi, M. 2016, ApJ, 821, 106
Vasquez, B. J., Smith, C. W., Hamilton, K., MacBride, B. T., & Leamon, R. J. 2007, JGRA, 112, A07101
Verdini, A., Velli, M., Matthaeus, W. H., Oughton, S., & Dmitruk, P. 2010, ApJL, 708, L116
Verth, G., Goossens, M., & He, J. S. 2011, ApJL, 733, L15
Withbroe, G. L. 1988, ApJ, 325, 442
Woolsey, L. N., & Cranmer, S. R. 2014, ApJ, 787, 160
Zank, G. P., Adhikari, L., Hunana, P., et al. 2017, ApJ, 835, 147
Zank, G. P., Adhikari, L., Hunana, P., et al. 2018, ApJ, 854, 32
Zank, G. P., Dosch, A., Hunana, P., et al. 2012, ApJ, 745, 35
Zank, G. P., le Roux, J. A., Webb, G. M., Dosch, A., & Khabarova, O. 2014, ApJ, 797, 28
Zank, G. P., & Matthaeus, W. H. 1992, JGR, 97, 17189
Zank, G. P., & Matthaeus, W. H. 1993, PhFl, 5, 257
Zank, G. P., Matthaeus, W. H., & Smith, C. W. 1996, JGR, 101, 17093
Zank, G. P., Nakanotani, M., Zhao, L. L., Adhikari, L., & Telloni, D. 2020, ApJ, 900, 115
Zaqarashvili, T. V., & Erdélyi, R. 2009, SSRv, 149, 355
Zhao, L.-L., Adhikari, L., Zank, G. P., Hu, Q., & Feng, X. S. 2018a, ApJ, 856, 94
Zhao, L. L., Zank, G. P., Adhikari, L., et al. 2020a, ApJS, 246, 26
Zhao, L. L., Zank, G. P., Adhikari, L., et al. 2020b, ApJ, 898, 113
Zhao, L. L., Zank, G. P., Chen, Y., et al. 2019, ApJ, 872, 4
Zhao, L. L., Zank, G. P., Khabarova, O., et al. 2018b, ApJL, 864, L34